

Synergy of Single Atoms Pd and Oxygen Vacancies on In_2O_3 for Highly Selective C1 Oxygenates Production from Methane under Visible Light

Lei Luo

Northwest University

Lei Fu

Northwest University

Huifen Liu

Northwest University

Youxun Xu

University College London

Jialiang Xing

Northwest University

Junwang Tang (✉ junwang.tang@ucl.ac.uk)

University College London <https://orcid.org/0000-0002-2323-5510>

Article

Keywords: methane conversion, single atom catalyst, methanol, defect engineering, photocatalysis

Posted Date: September 30th, 2021

DOI: <https://doi.org/10.21203/rs.3.rs-942037/v1>

License:   This work is licensed under a Creative Commons Attribution 4.0 International License.

[Read Full License](#)

Version of Record: A version of this preprint was published at Nature Communications on May 25th, 2022. See the published version at <https://doi.org/10.1038/s41467-022-30434-0>.

Abstract

Methane (CH₄) oxidation to high value chemicals under mild conditions through photocatalysis is a sustainable and appealing pathway, nevertheless confronting the critical issues on both conversion and selectivity. Herein, under visible irradiation (420 nm), the synergy of palladium (Pd) atom cocatalyst and oxygen vacancies (OVs) on In₂O₃ nanorods enabled superior photocatalytic CH₄ activation by O₂. The optimised catalyst reached ca. 100 μmol·h⁻¹ of C1 oxygenates, with a selectivity of primary products (CH₃OH and CH₃OOH) up to 82.5 %. Mechanism investigation elucidated that such superior photocatalysis was induced by the dedicated function of Pd single atoms and oxygen vacancies on boosting hole and electron transfer pathway, respectively. O₂ was proven to be the only oxygen source for CH₃OH production, while H₂O acted as the promoter for efficient CH₄ activation through ·OH production and facilitated product desorption as indicated by DFT modelling. This work thus provides new understandings on simultaneous regulation of activity and selectivity by the significant synergy of single atom cocatalysts and oxygen vacancies.

Introduction

As the predominant constituent of natural gas, methane hydrate and shale gas resources, selective methane (CH₄) oxidation to value-added chemicals holds considerable financial and environmental prospective [1–5]. However, the inert symmetrical tetrahedral structure of CH₄ makes it rather difficult for the dissociation of the first C-H bond, which is the most important step for activation of methane. [6–8] Industrial multistep route via steam reforming and subsequent Fischer-Tropsch synthesis could efficiently activate CH₄, while it requires harsh experimental conditions (eg. > 700 °C temperature and/or high pressure), causing huge energy-consumption and safety issues [9–13]. In parallel, it is relatively difficult to achieve high selectivity due to the more reactive characteristics of the desired oxygenates against both the reactant CH₄ and stable product CO₂. [14–17] Therefore, selective CH₄ conversion to value-added chemicals under mild conditions other than CO₂ is highly attractive, while confronting considerable challenges.

Photocatalysis offers an appealing alternative to drive many tough redox reactions under mild conditions including CO₂ conversion [18, 19], N₂ reduction[20] and selective CH₄ oxidation [8]. Recently, various value-added chemicals such as methanol [1, 21–23], formaldehyde [24, 25], ethanol [26, 27], ethane and ethylene [28–33] were produced by photocatalysis. For example, we found that up to 90 % selectivity with a yield of 3.5 μmol·h⁻¹ methanol could be achieved over the optimized FeO_x/TiO₂ photocatalyst under ambient condition using H₂O₂ as an oxidant [22]. Recently a high yield of liquid oxygenates including CH₃OH, CH₃OOH and HCHO were produced under full arc irradiation over Au supported ZnO, together with the good selectivity of primary products (CH₃OH and CH₃OOH) (< 70 %) [1]. Very recent, the yields of 18.7 μmol·h⁻¹ HCHO and 3.7 μmol·h⁻¹ CH₃OH were reported on quantum BiVO₄ with an excellent selectivity toward HCHO (87 %) and CH₃OH (99 %) under 300–400 nm or 400-780nm irradiation[25]. Given these

significant advances in photocatalytic methane conversion, the yield and/or selectivity to high value chemicals are still quite moderate, in particular it is very challenging to achieve methane activation under visible light irradiation instead of a full arc spectrum due to a narrowed bandgap with mitigated reduction or oxidation potentials

To realize visible driven methane oxidation by O_2 gas on narrow bandgap photocatalysts, cocatalyst is crucial that does not only promote charge separation, more importantly manipulates the activation energy of the methane conversion and the selectivity [34–39]. Furthermore rationally regulating the production of reactive oxygen species (ROS) through cocatalyst modification is necessary as $\cdot OH$ radicals have been widely regarded as the main species that induced CH_4 activation and over-oxidation [40, 41]. When CH_3OH served as the desired products, over-oxidation to $HCHO$ or CO_2 would be suppressed by lowering the oxidative potential of photogenerated hole through cocatalyst modification, thus improving the selectivity. Stimulated by molecular catalysis, single atom cocatalysts promise an extremely high efficiency, where atomic dispersed species with unsaturated coordination environment could improve the catalytic performances based on the unique electronic structure [42–44]. Meanwhile, high atom utilization efficiency could be achieved [45, 46]. On the other hand, since CH_4 exhibited low electron and proton affinity, moderate decoration of defective sites could enhance the chemical-adsorption of non-polar molecular, then promoting the activation of CH_4 [47]. Therefore, the integration of both defects and single atom cocatalyst decoration could boost charge separation, weaken oxidative potential and enhance CH_4 activation on a photocatalyst.

Herein, atomically dispersed palladium (Pd) supported on defective In_2O_3 was prepared and served as the visible-light responsive photocatalyst for CH_4 conversion to high value chemicals. Under 420 nm irradiation, the optimized production of oxygenates reached up to ca. 300 μmol in 3 h, with a very high selectivity of 82.5 % of the primary products. In-situ XPS and EPR spectra were conducted to investigate the charge transfer dynamics. The results indicated the dedicated roles of Pd atoms and oxygen vacancies (OVs) in promoting the transfer of photo-induced holes and electrons, respectively. DFT calculation results indicated H_2O could also promoted the desorption of the oxygenate products, thus suppressing over-oxidation and facilitate high selectivity of primary products. The introduction of atomic Pd and oxygen vacancies further enhanced this effect on suppressing over-oxidation. Isotopic labelled experiments further proved the methane conversion pathway.

Results And Discussion

Visible-light photocatalytic CH_4 oxidation by O_2

Atomic Pd cocatalyst was prepared by the in-situ photo-deposition method with K_2PdCl_4 and $(NH_4)_2PdCl_4$ as the precursors on the visible driven In_2O_3 nanorod photocatalyst. Two types of photocatalysts were synthesized as the defect-rich and defect-lean materials, denoted as Pd-def- In_2O_3 and Pd- In_2O_3 , respectively. For comparison, other noble metals including Pt and Au modified photocatalysts were also

prepared with the same dosage, denoted as M-(def)-In₂O₃ (M = Pt and Au). With different K₂PdCl₄ dosage, the as-prepared samples were denoted as Pd_x-def-In₂O₃, where x % represented the weight percentage of Pd to In₂O₃. In the following discussion, the best sample Pd-def-In₂O₃ and the reference Pd-In₂O₃ referred to Pd_{0.1}-def-In₂O₃ and Pd_{0.1}-In₂O₃ unless otherwise specified.

Typical noble metal cocatalysts (Pt, Pd, Au) loaded on In₂O₃ nanorods were first tested via photocatalytic CH₄ conversion with O₂ as the oxidant (**Figure 1a**). Under 420 nm irradiation, the products including CH₃OH, CH₃OOH and HCHO over Pd-In₂O₃ reaches 13.4, 32.3 and 27.5 μmol in 3 h reaction, respectively. The selectivity of the primary products (CH₃OH and CH₃OOH) was 62.1 % and the selectivity to the overoxidation products (HCHO and CO₂) was 37.9 %. In comparison, Au-In₂O₃ and Pt-In₂O₃ performed almost 100 % over-oxidized products (HCHO), with the trace yields of 1.4 and 0.9 μmol HCHO, respectively. Such differences suggested Pd cocatalyst was more suitable than Pt and Au for CH₄ activation to produce these primary products. The yield of oxygenates for Pd-In₂O₃ was improved further to 179.7 μmol by the introduction of defective sites to form Pd-def-In₂O₃, 2.5 times higher than that of Pd-In₂O₃ (73.2 μmol). Meanwhile, the selectivity of the primary products was improved from 62.1 % to 80.4 %, suggesting that deep-oxidation to HCHO and CO₂ was greatly suppressed under the synergy of Pd single atoms and oxygen vacancies (OVs). In the case of Au-def-In₂O₃ and Pt-def-In₂O₃, defect modification exhibited the similar phenomenon on promoting CH₄ conversion although the yield was much lower than that achieved on the Pd modified photocatalyst.

The effect of Pd single atoms was explored over Pd_x-def-In₂O₃. As shown in **Figure 1b**, Pd_x-def-In₂O₃ photocatalysts exhibited much higher oxygenates production than that of the pristine In₂O₃. With the raising of K₂PdCl₄ dosage, the production of the liquid oxygenates exhibited the volcanic trend, increasing from 48.7 μmol on Pd_{0.01}-def-In₂O₃ to 179.7 μmol on Pd_{0.1}-def-In₂O₃. Furthermore, the increasing K₂PdCl₄ dosage resulted in the decreased photocatalytic performance. Notably, the selectivity exhibited slight improvement from 76.5 % to 82.8 %. With a close look at the above results, OVs and Pd cocatalyst played the synergistic role in optimizing the activity and selectivity for photocatalytic CH₄ conversion.

Molar ratio of CH₄ to O₂ was tuned over Pd-def-In₂O₃ (**Figure 1c**). The production of oxygenates demonstrated the volcanic trend again, with the highest oxygenate production and selectivity achieved at 1 bar O₂ pressure. Reducing molar ratio of CH₄ to O₂ caused the decreased production to 116.0 μmol of primary products when CH₄/O₂ = 10/10, mainly ascribed to the decrease of CH₄ concentration. In parallel, the increased concentration of O₂ induced over-oxidation and decreased selectivity of the primary products from 80.4 % to 67.6 %. With the increase of H₂O dosage (**Figure 1d**), the production of oxygenates gradually increased, reaching the highest value with 100 mL H₂O dosage. The highest oxygenates achieved 299.0 μmol, 2.3 times improvement than that of 25 mL dosage (128.0 μmol) over Pd-def-In₂O₃. Moreover, the selectivity of the primary products improved from 74.2 to 82.5 % with H₂O

dosage increasing from 25 to 100 mL, which could be attributed to the enhanced desorption of the products from the surface of the photocatalyst when more water was used as discussed later. Notably, in the absence of H₂O dosage, CO₂ (8.5 μmol) was produced as the only product, suggesting the critical role of H₂O in promoting CH₄ activation as well suppressing over-oxidation, probably ascribed to the production of ·OH radical and promotion desorption of oxygenates by H₂O [48]. While increasing the total pressure of the gaseous reactants, CH₄ dissolved increased and the oxygenate production gradually increased (**Figure 1e**), e.g. only trace amount of HCHO (4.1 μmol) produced at 1 bar and reaching the highest yield of 179.7 μmol when the pressure was 20 bar. To investigate the stability of the optimized photocatalyst, we carried out the cycling test experiment over Pd-def-In₂O₃ photocatalyst. No obvious decrease of oxygenates was observed under 15 hours reaction (**Figure 1f**), demonstrating the good stability of Pd-def-In₂O₃.

Structural identification

X-ray diffraction (XRD) patterns were recorded to probe the crystalline structure of the representative photocatalysts (In₂O₃, Pd-In₂O₃ and Pd-def-In₂O₃) (**Figure S1**). The diffraction peaks on all three samples at 30.7°, 35.5°, 51.0° and 60.7° were well matched with the standard phase of In₂O₃ (PDF#71-2194). While no Pd and PdO_x diffraction peaks were observed on Pd-In₂O₃ and Pd-def-In₂O₃, indicating the high dispersion of Pd species. The slightly weakened relative intensity from 100 % of In₂O₃ to 97 % and 93 % of Pd-In₂O₃ and Pd-def-In₂O₃ could be probably ascribed to the introduction of defects. Raman spectra (**Figure 2a**) further supported the well-established In₂O₃ phase. The typical Raman peaks for In₂O₃ were clearly observed at 130.6, 305.1 and 494.8 cm⁻¹ [49]. For Pd-In₂O₃ and Pd-def-In₂O₃, the dominant peak exhibited a slight left-shift from 130.6 to 129.9 cm⁻¹, attributed to the surface strain effect induced by the Pd cocatalyst deposition [50].

Electron paramagnetic resonance (EPR) spectra were conducted to evaluate the spin-electrons including oxygen vacancies (**Figure 2b**). For the pristine In₂O₃ and Pd-In₂O₃, a single Lorentz peak at g = 1.882 was observed, ascribed to the electrons on the conduction band (CB) [51, 52]. In the case of Pd-def-In₂O₃, the signal of this peak exhibited much stronger intensity than the others, suggesting the higher electron density on CB. Meanwhile, an additional Lorentz peak was observed at g = 2.001, which could be attributed to the free-electrons trapped by the oxygen vacancies [52], thus suggesting the existence of oxygen vacancies in Pd-def-In₂O₃. The introduction of oxygen vacancies might contribute to the stronger EPR peak at g = 1.882.

High-resolution transmission electron microscope (HRTEM) images further proved the defective structure of Pd-def-In₂O₃ (**Figure 2c-d**). Pd-def-In₂O₃ reserved the nanorod morphology with dimension of 203 nm in diameter and 1450 nm in length (insert of **Figure 2c**) as that of the In₂O₃ substrate and Pd-In₂O₃ (**Figure S2**). In addition, a thin amorphous/defective layer of ca. 4 nm was observed on the edge (**Figure**

2d). The bulk crystal plane distance of 0.415 nm was indexed to the (211) facet of In_2O_3 . On the contrary, there is not such defective layer as indicated in **Figure S2b**. Elemental distribution of the corresponding area was analysed by the EDS-mapping images (**Figure 2e**). Obviously, Pd-def- In_2O_3 exhibited uniform palladium distribution with indium and oxygen elements. The aberration corrected HAADF-STEM image in **Figure 2f** clearly indicated the atomic distribution of Pd, where the weak intensity spots cycled by the yellow corresponded to Pd atoms. The x-y line scan along the yellow rectangle of **Figure 2f** clearly presents the atomic dispersion of Pd as shown in **Figure 2g**. Therefore the best sample was composed of single atom Pd and oxygen vacancies on In_2O_3 nanorods.

Mechanism investigation

UV-vis diffuse reflection spectra (UV-DRS) were conducted to evaluate the photoabsorption ability of the representative photocatalysts (In_2O_3 , Pd- In_2O_3 and Pd-def- In_2O_3) (**Figure 3a**). All the three photocatalysts exhibited the similar photoabsorption onset at ca. 450 nm, indicating that the modification of single atom Pd and OVs has little influence on bandgap energy and bandgap energy was not the decisive reason that induced improvement of photocatalysis.

In-situ high-resolution Pd_{3d} X-ray photoelectric spectra (XPS) in dark and under light were conducted to study the charge transfer direction of Pd-def- In_2O_3 (**Figure 3b** and **Figure S3**). In dark, the $\text{Pd}_{3d5/2}$ XPS peak could be deconvoluted into two binding peaks at 336.55 and 335.38 eV, which were assigned to the Pd^{2+} and Pd^0 species, respectively [53]. Under light irradiation, the peak exhibited a left-shift to higher binding energy (**Figure S3**). Further deconvoluted results (**Figure 3b**) suggested that Pd^{2+} content increased to 26.3 %, much higher than 6.9 % in dark. Such increased Pd^{2+} content suggested Pd served as the hole acceptors upon excitation. In-situ EPR spectra under light were conducted to evaluate the role of OVs. As shown in **Figure 3c**, the signal at $g = 2.0009$ was attributed to the electrons trapped by the oxygen vacancies, which performed gradually increasing intensity from 100 % to 226 % with the prolonged irradiation to 360 seconds. This stronger EPR intensity suggested a higher concentration of spin-electrons and thus demonstrated OVs served as the electron acceptor [54]. Therefore, single atom Pd and OVs separately acted as the hole and electron acceptors under light irradiation, which would greatly contribute to the enhanced charge separation.

Photocurrent responses (**Figure S4**) were tested to evaluate the charge separation efficiency. Pristine In_2O_3 exhibited a relatively low photocurrent density of $61.8 \mu\text{A}\cdot\text{cm}^{-2}$. After photo-depositing high dispersed Pd cocatalyst, Pd- In_2O_3 nearly doubled photocurrent density to $120.6 \mu\text{A}\cdot\text{cm}^{-2}$. The photocurrent density was further improved to $168.1 \mu\text{A}\cdot\text{cm}^{-2}$ on Pd-def- In_2O_3 , almost 2.7 and 1.4 times enhancement than that of In_2O_3 and Pd- In_2O_3 , respectively. Such highest photocurrent density on Pd-def- In_2O_3 attributed to the most efficient charge separation, indicating the defects and single atom Pd could greatly enhance charge transfer, which is consistent with the analysis mentioned above. Steady-state

fluorescence (PL) spectra further evidenced the enhanced charge separation efficiency. As shown in **Figure 3d**, a relatively strong PL emission peak was observed for the pristine In_2O_3 , attributed to the severe charge recombination. In comparison, the PL intensity for $\text{Pd-In}_2\text{O}_3$ was greatly weakened, indicating the suppressed charge recombination. For $\text{Pd-def-In}_2\text{O}_3$ photocatalyst, the most weakened PL peak were observed, ascribed to the most enhanced charge separation efficiency, which was corresponding with the photocurrent analysis. Time-decay PL spectra were conducted to evaluate the PL lifetime. As shown in **Figure S5**, $\text{Pd-def-In}_2\text{O}_3$ photocatalyst exhibited the slowest PL decay kinetics. The fitting results (**Table S1**) showed that $\text{Pd-def-In}_2\text{O}_3$ exhibited the average PL lifetime at 4.99 ns, longer than that of In_2O_3 (3.60 ns) and $\text{Pd-In}_2\text{O}_3$ (4.28 ns), which would be beneficial to the efficient utilization of separated charge carriers.

Reactive oxygen species including $\cdot\text{OOH}$ and $\cdot\text{OH}$ radicals were widely regarded as the main active species for CH_4 activation [55] and monitored by in-situ EPR spectra with 5, 5-dimethyl-1-pyrroline N-oxide (DMPO) as the spin-electron trapping agents. As shown in **Figure 4a**, the DMPO-OOH adduct was detected under light over different photocatalysts and ascribed to the presence of $\cdot\text{OOH}$, which came from the reduction of O_2 molecule with photo-induced electrons and H^+ . A stronger intensity of DMPO-OOH was observed for $\text{Pd-def-In}_2\text{O}_3$, suggesting the production of $\cdot\text{OOH}$ radical was enhanced by the integration of single atom Pd and OVs. On the other hand, in-situ EPR spectra under light was used to monitor the generation of $\cdot\text{OH}$ radical with DMPO as the trapping agent in H_2O . The 1:2:2:1 quartet signals were observed and assigned to the DMPO-OH adduct, suggesting the generation of $\cdot\text{OH}$ radical (**Figure 4b**). It was obvious that $\text{Pd-def-In}_2\text{O}_3$ produced much more $\cdot\text{OH}$ under identical conditions than $\text{Pd-In}_2\text{O}_3$ and In_2O_3 was the worse. It is believed that $\cdot\text{OH}$ initially activates CH_4 to methyl radical ($\cdot\text{CH}_3$), thus $\text{Pd-def-In}_2\text{O}_3$ performed CH_4 activation best followed by $\text{Pd-In}_2\text{O}_3$, which is consistent with the step by step enhanced photocatalytic performances by Pd and then both Pd and oxygen vacancies, indicating that oxygen vacancies could promote charge separation and also facilitate water oxidation reaction on Pd. Coumarin was used as the probe for $\cdot\text{OH}$ radical detection due to the easy reaction between coumarin and $\cdot\text{OH}$ to produce 7-hydroxycoumarin (7-HC) that could be detected by UV-vis spectra at 412 nm (**Figure 4c**). The results further supported that $\text{Pd-def-In}_2\text{O}_3$ held the strongest ability for $\cdot\text{OH}$ production, which facilitated CH_4 activation. Therefore, single atom Pd worked as the hole acceptor, which then catalysed $\cdot\text{OH}$ radical production from water oxidation. Simultaneously, OVs acted as the electron acceptor, which then catalysed O_2 reduction to generate $\cdot\text{OOH}$ radical.

The reaction pathway was investigated by isotopic labelled experiments, including using H_2^{18}O and $^{18}\text{O}_2$. In the presence of 3 mL H_2^{18}O , 1 bar $^{16}\text{O}_2$ and 19 bar CH_4 , no isotopic labelled $\text{CH}_3^{18}\text{OH}$ ($m/z = 33$ and 34) was detected by GCMS (**Figure 4d**), suggesting H_2O was not the oxygen source that directly participated the formation of oxygenates. In parallel, when using 3 mL H_2^{16}O , 1 bar $^{18}\text{O}_2$ and 19 bar CH_4 , the signals at $m/z = 34$ and 33 were attributed to the isotopic labelled $\text{CH}_3^{18}\text{OH}$ and its fragment (**Figure 4d**), suggesting O_2 was the only oxygen source for CH_3OH formation. Carbon source for methanol

production were also studied in the presence of 5 bar isotopic labelled $^{13}\text{CH}_4$ (**Figure 4e**), where the signal of mass spectra (MS) at $m/z = 33$ was ascribed to $^{13}\text{CH}_3\text{OH}$, demonstrating that CH_4 was the carbon source for oxygenates production.

DFT calculations (**Figure 5**) were conducted to explain the improved selectivity of primary products. It should be noted that timely desorption of the primary products on the active sites could efficiently avoid its deep-oxidation to HCHO and CO_2 . As $\cdot\text{OH}$ radical was regarded as the main species that induced oxidation on single atom Pd cocatalyst, it was accordingly considered that the efficient desorption of primary products like CH_3OH on Pd is critical to suppress further oxidation. Thus, the adsorption energies of H_2O and CH_3OH were calculated since the stronger adsorption of H_2O might promote the desorption of CH_3OH . H_2O and CH_3OH adsorption on In_2O_3 and on Pd/ In_2O_3 were modelled and optimized by the density functional theory (DFT) calculations. As shown in **Figure 5a** and **b**, the adsorption energies of H_2O on In_2O_3 , Pd- In_2O_3 and Pd-def- In_2O_3 were -0.76, -1.57 and -2.14 eV, respectively, much larger than the CH_3OH adsorption energy of -0.47, -1.38 and -1.50 eV on the specified model. Such larger adsorption energies indicate CH_3OH could be easily replaced by H_2O on In_2O_3 or Pd atoms, promoting the desorption of CH_3OH . Moreover, adsorption energies further increased with the introduction of both Pd atom and oxygen vacancy, demonstrating such co-modification of Pd atoms and OVs could promote the adsorption of H_2O most efficiently, which is consistent with the increased production of $\cdot\text{OH}$ radicals as analyzed by the in-situ EPR and coumarin experiments. Though the adsorption of CH_3OH was also enhanced due to the introduction of Pd atoms and OVs, H_2O adsorption energy was enhanced much more, thus water could facilitate the desorption of primary products and avoid overoxidation as indicated in **Figure 1d**.

Based on the above results, aerobic photocatalytic CH_4 conversion mechanism over Pd-def- In_2O_3 was proposed (**Scheme 1**). Generally, under 420 nm irradiation, electrons (e^-) were excited to the conduction band of In_2O_3 nanorod photocatalyst, while leaving holes (h^+) on the valence band. Then the photo-induced electrons were trapped by the oxygen vacancies, activating O_2 with H^+ to produced $\cdot\text{OOH}$ radicals as detected by the in-situ EPR spectra. In parallel, Pd atoms served as the hole acceptors ($\text{Pd} + h^+ \rightarrow \text{Pd}^{\delta+}$), and then reacted with the adsorbed H_2O to produced $\cdot\text{OH}$ ($\text{Pd}^{\delta+} + \text{H}_2\text{O} \rightarrow \text{Pd}^0 + \cdot\text{OH} + \text{H}^+$). CH_4 molecules were next activated by the as-produced $\cdot\text{OH}$ to $\cdot\text{CH}_3$. The coupling reaction between $\cdot\text{CH}_3$ and $\cdot\text{OOH}$ then generated the primary products (CH_3OOH), and subsequently transferred to CH_3OH as indicated in **Scheme 1b**. Compared with the pristine In_2O_3 , the incorporation of Pd single atoms significantly promoted charge separation and facilitated the generation of reactive species, thus promoting CH_4 conversion to oxygenates. Pd atoms loading also moderated the oxidation ability of photoinduced holes on In_2O_3 as indicated in **Scheme 1a**, reducing the overoxidation of the primary products. Further decoration of oxygen vacancies could strengthen the promoted charge separation efficiency, which eventually resulted in the superior photocatalytic CH_4 conversion activity and selectivity. In order to suppress over-oxidation, it was also critical to enhance the desorption of primary oxygenate products by H_2O , as supported by the DFT calculation.

In summary, visible-light-driven CH₄ conversion at ambient temperature was reported over the In₂O₃ nanorod photocatalyst with loading of Pd single atoms cocatalysts and oxygen vacancies. Under 420 nm irradiation, superior yield (99.7 μmol·h⁻¹) and selectivity (82.5 %) of the primary products were achieved on Pd-def-In₂O₃ photocatalyst under optimized reaction conditions. In-situ XPS and EPR spectra under visible light irradiation indicated that Pd and oxygen vacancies acted as the hole and electron acceptors, respectively, thus synergistically boosted charge separation and transfer. Isotopic labelled experiment proved that O₂ was the only oxygen source for oxygenates production, while H₂O was the promoter of CH₄ activation through the production of ·OH radical as monitored by the in-situ EPR spectra with DMPO as the spin-trapping agent. DFT calculation results suggested that H₂O performed much larger adsorption energies than CH₃OH on either In₂O₃, def-In₂O₃ or Pd-def-In₂O₃, suggesting the stronger adsorption of H₂O than CH₃OH, which was beneficial to the timely desorption of the produced CH₃OH, thus avoiding further over-oxidation. The introduction of Pd and oxygen vacancies could further improve the selectivity of primary oxygenates mainly through the greatly enhanced adsorption of H₂O and the reduced oxidation potential of photoinduced holes. This work provided an useful avenue on co-modification by oxidative single atom cocatalyst and oxygen vacancies for simultaneous regulation of both activity and selectivity through enhancing charge separation, moderated photohole oxidation ability and timely promoted desorption of primary products by a solvent.

Methods

Synthesis of In₂O₃ nanorods

In₂O₃ nanorods were prepared according to the previous study [56]. Typically, 12.0 g urea and 1.5 g InCl₃ were dissolved in 135 g H₂O, followed by stirring at 80 °C for 14 h. After naturally cooling down, the reactant was centrifuged and washed with H₂O for several times. The white powder was then dried in vacuum at 60 °C overnight. After thermal-treating in air at 700 °C for 5 h at a ramping rate of 5 °C·min⁻¹, yellow powder was obtained and denoted as In₂O₃.

Synthesis of Pd_x-In₂O₃ and Pd_x-def-In₂O₃ nanorods

Pd_x-In₂O₃ and Pd_x-def-In₂O₃ nanorods were prepared through photo-deposition with ammonium tetrachloropalladate(II) ((NH₄)₂PdCl₄) and potassium tetrachloropalladate(II) (K₂PdCl₄) as the precursors, respectively. The synthesis was conducted in the multichannel reactor (*Beijing Perfectlight Technology Co., Ltd*). For Pd_x-def-In₂O₃ preparation, 200 mg In₂O₃ was first dispersed through sonication with the aqueous solution containing 10 vol.% methanol. Then certain amount of K₂PdCl₄ solution was added. After sealing and purging with ultrapure argon (99.999 vol.%) for 30 min, the reactor was bottom-irradiated for 3 h to facilitate Pd photo-deposition. The suspension was then centrifuged, washed with H₂O for several times and dried under vacuum at 60 °C overnight. The as-prepared samples were denoted as Pd_x-def-In₂O₃, where x % represented the mass percentage of palladium to In₂O₃ substrates. Pd_x-In₂O₃

with no oxygen vacancies was prepared under identical conditions except the usage of $(\text{NH}_4)_2\text{PdCl}_4$ instead of K_2PdCl_4 .

Characterizations

XRD were measured to obtain the crystalline structure on the *D8 ADVANCE* diffractometer (*Bruker Co., Ltd*). Palladium and potassium contents were measured through inductively coupled plasma atomic emission spectrometry (ICP-AES) on the *Agilent 7900 ICP-MS* instrument. Raman spectra were collected on the *DXR 2DXR2* instrument (*Thermo Fisher Scientific, Co., Ltd*). HRTEM images were captured on the *Talos F200X* instrument (*FEI Co., Ltd*). UV-DRS spectra were measured on the UV-3600 plus spectrophotometer (*Shimadzu Co., Ltd*). Photocurrent test was conducted on the electronic workstation (*CHI660E*) on the three-electrode system. Ag/AgCl electrode, platinum sheet electrode and Na_2SO_4 solution (0.1 M) were used as the reference electrode, counter electrode and electrolyte, respectively. The mixtures of photocatalyst, ethanol and Nifion solution (*Shanghai Adamas Reagent Co., Ltd*) were suspended and sonicated to prepare the working electrode. In-situ XPS in dark and under light were measured on the *Thermo ESCALAB 250Xi* instrument with an Al K α radiation source. In-situ solid-state EPR spectra in dark and under light were measured with 20 mg photocatalyst on the *ELEXSYS II* EPR instrument.

Photocatalytic CH_4 conversion

Photocatalytic CH_4 conversion was conducted in a top-irradiated high-pressure reactor with 200 mL volume. LED lamp (420 nm, *PLS-LED100C, Beijing Perfectlight Technology Co., Ltd*) was used as the light source. Typically, 20 mg photocatalyst was dispersed in 50 mL distilled water. After sealing and purging with ultrapure O_2 (99.999 vol.%) for 20 min, 1 bar O_2 and 19 bar CH_4 (99.999 vol.%) were flowed into the reactor. The temperature of the reactor was maintained at 25 °C by the cold-water bath. After reacting for 3 h, the gaseous and liquid products like methanol were measured by the gas chromatography (*GC2014, Shimadzu Co., Ltd*) equipped with thermal conductivity detector (TCD) and flame ionization detector (FID). CH_3OOH and CH_3OH were measured through ^1H nuclear magnetic resonance (NMR) (*AVANCE III, JEOL Ltd*). As CH_3OOH and CH_3OH have the same number of methyl, the area ratio of CH_3OOH to CH_3OH in ^1H NMR should be the molar ratio of CH_3OOH to CH_3OH . Thus, CH_3OOH could be quantified. HCHO was measured through the colorimetric method [57] on the *UV-3600 Plus* spectrometer (*Shimadzu Co., Ltd*).

Isotope labelling experiments

For carbon source investigation: 20 mg Pd-def- In_2O_3 photocatalyst was dispersed in 3 mL H_2O . After the reactor being degassed for 30 min, 1 bar O_2 and 5 bar $^{13}\text{CH}_4$ were injected into the reactor. After reacting for 6 h, the suspension was filtered and then the solvent was analysed by GC-MS (QP2010, *Shimadzu Co., Ltd*) equipped with the Cap WAX column.

For oxygen source investigation: 20 mg Pd-def-In₂O₃ photocatalyst was dispersed in 3 mL H₂¹⁶O or H₂¹⁸O. After the reactor being degassed for 30 min, 1 bar ¹⁸O₂ or ¹⁶O₂ and 5 bar CH₄ were injected into the reactor. After reacting for 6 h, the suspension was filtered and then the solvent was analysed by GC-MS (QP2010, Shimadzu Co., Ltd).

Monitor of the reactive species

DMPO was used as the spin-trapping agent for monitor of the reactive species including ·OOH and ·OH radicals. For ·OOH radical detection, 10 mg Pd-def-In₂O₃ photocatalyst was dispersed into 5 mL DMPO/methanol solution. After purging with ultrapure O₂ (99.999 vol.%) for 20 min, in-situ EPR spectra in dark and under light irradiation were collected. For ·OH radical detection, 10 mg Pd-def-In₂O₃ photocatalyst was dispersed in 5 mL aqueous DMPO solution. After purging with ultrapure O₂ (99.999 vol.%) for 20 min, in-situ EPR spectra in dark and under light were collected.

Analysis of hydroxyl radical (·OH)

Coumarin was used as the probe for the quantification of ·OH via the production of 7-HC [40]. Typically, 20 mg photocatalyst was dispersed in 100 mL aqueous coumarin solution (5×10⁻⁴ M). After stirring for 30 min in dark, the suspension was irradiated with the LED light source (420 nm, PLS-LED100C, Beijing Perfectlight Technology Co., Ltd). Certain amount of suspension was sampled and filtered in the 10 min intervals. PL intensity of the produced 7-HC in the solution was then measured on the F4500 spectrofluorometer.

DFT calculation of adsorption energies

The first-principles were employed to perform all the density functional theory (DFT) calculations within the generalized gradient approximation (GGA) using the PBE formulation. The projected augmented wave (PAW) potentials have been chosen to describe the ionic cores and take valence electrons into account using a plane wave basis set with a kinetic energy cutoff of 400 eV. Partial occupancies of the Kohn-Sham orbitals were allowed using the Gaussian smearing method and a width of 0.05 eV. The electronic energy was considered self-consistent when the energy change was smaller than 10⁻⁴ eV. A geometry optimization was considered convergent when the force change was smaller than 0.05 eV/Å. Grimme's DFT-D3 methodology was applied to describe the dispersion interactions. Three models including In₂O₃ with (111) facet, def-In₂O₃ with one oxygen vacancy and Pd-def-In₂O₃ with both one oxygen vacancy and single atom Pd modification were conducted. During structural optimizations, the 2×2×1 Monkhorst-Pack k-point grid for Brillouin zone was used for k-point sampling for structures. Finally, the adsorption energies (E_{ads}) were calculated as $E_{ads} = E_{ad/sub} - E_{ad} - E_{sub}$, where $E_{ad/sub}$, E_{ad} , and E_{sub} were the total energies of the optimized adsorbate/substrate system, the adsorbate in the structure, and the clean substrate, respectively.

Data availability

The data that support the findings of this study are available from the corresponding author upon reasonable request.

References

- [1] Song, H., X. Meng, S. Wang, W. Zhou, X. Wang, T. Kako, and J. Ye. Direct and Selective Photocatalytic Oxidation of CH₄ to Oxygenates with O₂ on Cocatalysts/ZnO at Room Temperature in Water. *Journal of the American Chemical Society*, **2019**, *141*, 20507.
- [2] Sushkevich, V.L., D. Palagin, M. Ranocchiari, and J.A.v. Bokhoven. Selective Anaerobic Oxidation of Methane Enables Direct Synthesis of Methanol. *Science*, **2017**, *356*, 523.
- [3] Sher Shah, M.S.A., C. Oh, H. Park, Y.J. Hwang, M. Ma, and J.H. Park. Catalytic Oxidation of Methane to Oxygenated Products: Recent Advancements and Prospects for Electrocatalytic and Photocatalytic Conversion at Low Temperatures. *Advanced Science*, **2020**, *7*, 2001946.
- [4] Hu, D., V.V. Ordonsky, and A.Y. Khodakov. Major Routes in the Photocatalytic Methane Conversion into Chemicals and Fuels under Mild Conditions. *Applied Catalysis B: Environmental*, **2021**, *286*, 119913.
- [5] Meyet, J., K. Searles, M.A. Newton, M. Wörle, A.P. van Bavel, A.D. Horton, J.A. van Bokhoven, and C. Copéret. Monomeric Copper(II) Sites Supported on Alumina Selectively Convert Methane to Methanol. *Angewandte Chemie International Edition*, **2019**, *58*, 9841.
- [6] Ravi, M., M. Ranocchiari, and J.A. van Bokhoven. The Direct Catalytic Oxidation of Methane to Methanol—a Critical Assessment. *Angewandte Chemie International Edition*, **2017**, *56*, 16464.
- [7] Zakaria, Z. and S.K. Kamarudin. Direct Conversion Technologies of Methane to Methanol: An Overview. *Renewable and Sustainable Energy Reviews*, **2016**, *65*, 250.
- [8] Song, H., X. Meng, Z.-j. Wang, H. Liu, and J. Ye. Solar-Energy-Mediated Methane Conversion. *Joule*, **2019**, *3*, 1606.
- [9] Agarwal, N., S.J. Freakley, R.U. McVicker, S.M. Althahban, N. Dimitratos, Q. He, D.J. Morgan, R.L. Jenkins, D.J. Willock, S.H. Taylor, C.J. Kiely, and G.J. Hutchings. Aqueous Au-Pd Colloids Catalyze Selective CH₄ Oxidation to CH₃OH with O₂ under Mild Conditions. *Science*, **2017**, *358*, 223.
- [10] Hammond, C., M.M. Forde, M.H. Ab Rahim, A. Thetford, Q. He, R.L. Jenkins, N. Dimitratos, J.A. Lopez-Sanchez, N.F. Dummer, D.M. Murphy, A.F. Carley, S.H. Taylor, D.J. Willock, E.E. Stangland, J. Kang, H. Hagen, C.J. Kiely, and G.J. Hutchings. Direct Catalytic Conversion of Methane to Methanol in an Aqueous Medium by Using Copper-Promoted Fe-ZSM-5. *Angewandte Chemie International Edition*, **2012**, *51*, 5129.

- [11] Okolie, C., Y.F. Belhseine, Y. Lyu, M.M. Yung, M.H. Engelhard, L. Kovarik, E. Stavitski, and C. Sievers. Conversion of Methane into Methanol and Ethanol over Nickel Oxide on Ceria-Zirconia Catalysts in a Single Reactor. *Angewandte Chemie International Edition*, **2017**, *56*, 13876.
- [12] Ma, J., K. Mao, J. Low, Z. Wang, D. Xi, W. Zhang, H. Ju, Z. Qi, R. Long, X. Wu, L. Song, and Y. Xiong. Efficient Photoelectrochemical Conversion of Methane into Ethylene Glycol by WO_3 Nanobar Arrays. *Angewandte Chemie International Edition*, **2021**, *60*, 9357.
- [13] Zhou, Y., H. Wang, X. Liu, S. Qiao, D. Shao, J. Zhou, L. Zhang, and W. Wang. Direct Piezocatalytic Conversion of Methane into Alcohols over Hydroxyapatite. *Nano Energy*, **2021**, *79*, 105449.
- [14] Schwach, P., X. Pan, and X. Bao. Direct Conversion of Methane to Value-Added Chemicals over Heterogeneous Catalysts: Challenges and Prospects. *Chemical Reviews*, **2017**, *117*, 8497.
- [15] Tian, J., J. Tan, Z. Zhang, P. Han, M. Yin, S. Wan, J. Lin, S. Wang, and Y. Wang. Direct Conversion of Methane to Formaldehyde and CO on B_2O_3 Catalysts. *Nature Communications*, **2020**, *11*, 5693.
- [16] Yu, T., Z. Li, L. Lin, S. Chu, Y. Su, W. Song, A. Wang, B.M. Weckhuysen, and W. Luo. Highly Selective Oxidation of Methane into Methanol over Cu-Promoted Monomeric Fe/ZSM-5. *ACS Catalysis*, **2021**, *11*, 6684.
- [17] Jin, Z., L. Wang, E. Zuidema, K. Mondal, M. Zhang, J. Zhang, C. Wang, X. Meng, H. Yang, C. Mesters, and F.-S. Xiao. Hydrophobic Zeolite Modification for in Situ Peroxide Formation in Methane Oxidation to Methanol. *Science*, **2020**, *367*, 193.
- [18] Wang, Y., X. Liu, X. Han, R. Godin, J. Chen, W. Zhou, C. Jiang, J.F. Thompson, K.B. Mustafa, S.A. Shevlin, J.R. Durrant, Z. Guo, and J. Tang. Unique Hole-Accepting Carbon-Dots Promoting Selective Carbon Dioxide Reduction Nearly 100% to Methanol by Pure Water. *Nature Communications*, **2020**, *11*, 2531.
- [19] Wang, Y., R. Godin, J.R. Durrant, and J. Tang. Efficient Hole Trapping in Carbon Dot/Oxygen-Modified Carbon Nitride Heterojunction Photocatalysts for Enhanced Methanol Production from CO_2 under Neutral Conditions. *Angewandte Chemie International Edition*, **2021**, *60*, 20811.
- [20] Han, Q., C. Wu, H. Jiao, R. Xu, Y. Wang, J. Xie, Q. Guo, and J. Tang. Rational Design of High-Concentration Ti^{3+} in Porous Carbon-Doped TiO_2 Nanosheets for Efficient Photocatalytic Ammonia Synthesis. *Adv Mater*, **2021**, *33*, e2008180.
- [21] Zhou, W., X. Qiu, Y. Jiang, Y. Fan, S. Wei, D. Han, L. Niu, and Z. Tang. Highly Selective Aerobic Oxidation of Methane to Methanol over Gold Decorated Zinc Oxide Via Photocatalysis. *Journal of Materials Chemistry A*, **2020**, *8*, 13277.

- [22] Xie, J., R. Jin, A. Li, Y. Bi, Q. Ruan, Y. Deng, Y. Zhang, S. Yao, G. Sankar, D. Ma, and J. Tang. Highly Selective Oxidation of Methane to Methanol at Ambient Conditions by Titanium Dioxide-Supported Iron Species. *Nature Catalysis*, **2018**, *1*, 889.
- [23] Feng, N., H. Lin, H. Song, L. Yang, D. Tang, F. Deng, and J. Ye. Efficient and Selective Photocatalytic CH₄ Conversion to CH₃OH with O₂ by Controlling Overoxidation on TiO₂. *Nature Communications*, **2021**, *12*, 10.1038/s41467-021-24912-0.
- [24] Wei, S., X. Zhu, P. Zhang, Y. Fan, Z. Sun, X. Zhao, D. Han, and L. Niu. Aerobic Oxidation of Methane to Formaldehyde Mediated by Crystal-O over Gold Modified Tungsten Trioxide Via Photocatalysis. *Applied Catalysis B: Environmental*, **2021**, *283*, 119661.
- [25] Fan, Y., W. Zhou, X. Qiu, H. Li, Y. Jiang, Z. Sun, D. Han, L. Niu, and Z. Tang. Selective Photocatalytic Oxidation of Methane by Quantum-Sized Bismuth Vanadate. *Nature Sustainability*, **2021**, *4*, 509.
- [26] Zhou, Y., L. Zhang, and W. Wang. Direct Functionalization of Methane into Ethanol over Copper Modified Polymeric Carbon Nitride Via Photocatalysis. *Nature Communications*, **2019**, *10*, 506.
- [27] Yang, Z., Q. Zhang, L. Ren, X. Chen, D. Wang, L. Liu, and J. Ye. Efficient Photocatalytic Conversion of CH₄ into Ethanol with O₂ over Nitrogen Vacancy-Rich Carbon Nitride at Room Temperature. *Chemical Communications*, **2021**, *57*, 871.
- [28] Yu, X., V.L. Zholobenko, S. Moldovan, D. Hu, D. Wu, V.V. Ordonsky, and A.Y. Khodakov. Stoichiometric Methane Conversion to Ethane Using Photochemical Looping at Ambient Temperature. *Nature Energy*, **2020**, *5*, 511.
- [29] Li, X., J. Xie, H. Rao, C. Wang, and J. Tang. Pt and Cu_xO Decorated TiO₂ Photocatalyst for Oxidative Coupling of Methane to C₂ Hydrocarbons in a Flow Reactor. *Angewandte Chemie International Edition*, **2020**, *59*, 19702.
- [30] Ishimaru, M., F. Amano, C. Akamoto, and S. Yamazoe. Methane Coupling and Hydrogen Evolution Induced by Palladium-Loaded Gallium Oxide Photocatalysts in the Presence of Water Vapor. *Journal of Catalysis*, **2021**, *397*, 192.
- [31] Yu, L., Y. Shao, and D. Li. Direct Combination of Hydrogen Evolution from Water and Methane Conversion in a Photocatalytic System over Pt/TiO₂. *Applied Catalysis B: Environmental*, **2017**, *204*, 216.
- [32] Chen, Z., S. Wu, J. Ma, S. Mine, T. Toyao, M. Matsuoka, L. Wang, and J. Zhang. Non-Oxidative Coupling of Methane: N-Type Doping of Niobium Single Atoms in TiO₂-SiO₂ Induces Electron Localization. *Angewandte Chemie International Edition*, **2021**, *60*, 11901.
- [33] Li, N., R. Jiang, Y. Li, J. Zhou, Q. Ma, S. Shen, and M. Liu. Plasma-Assisted Photocatalysis of CH₄ and CO₂ into Ethylene. *ACS Sustainable Chemistry & Engineering*, **2019**, *7*, 11455.

- [34] Cho, Y., B. Park, D.K. Padhi, I.A.M. Ibrahim, S. Kim, K.H. Kim, K.-S. Lee, C.-L. Lee, J.W. Han, S.H. Oh, and J.H. Park. Disordered-Layer-Mediated Reverse Metal–Oxide Interactions for Enhanced Photocatalytic Water Splitting. *Nano Letters*, **2021**, 10.1021/acs.nanolett.1c01368.
- [35] Ma, J., X. Tan, Q. Zhang, Y. Wang, J. Zhang, and L. Wang. Exploring the Size Effect of Pt Nanoparticles on the Photocatalytic Nonoxidative Coupling of Methane. *ACS Catalysis*, **2021**, *11*, 3352.
- [36] Song, H., X. Meng, S. Wang, W. Zhou, S. Song, T. Kako, and J. Ye. Selective Photo-Oxidation of Methane to Methanol with Oxygen over Dual-Cocatalyst-Modified Titanium Dioxide. *ACS Catalysis*, **2020**, *10*, 14318.
- [37] Chen, F., T. Ma, T. Zhang, Y. Zhang, and H. Huang. Atomic-Level Charge Separation Strategies in Semiconductor-Based Photocatalysts. *Advanced Materials*, **2021**, *33*, 2005256.
- [38] Ling, T., M. Jaroniec, and S.-Z. Qiao. Recent Progress in Engineering the Atomic and Electronic Structure of Electrocatalysts Via Cation Exchange Reactions. *Advanced Materials*, **2020**, *32*, 2001866.
- [39] Lee, B.-H., S. Park, M. Kim, A.K. Sinha, S.C. Lee, E. Jung, W.J. Chang, K.-S. Lee, J.H. Kim, S.-P. Cho, H. Kim, K.T. Nam, and T. Hyeon. Reversible and Cooperative Photoactivation of Single-Atom Cu/TiO₂ Photocatalysts. *Nature Materials*, **2019**, *18*, 620.
- [40] Nosaka, Y. and A.Y. Nosaka. Generation and Detection of Reactive Oxygen Species in Photocatalysis. *Chemical Reviews*, **2017**, *117*, 11302.
- [41] Xiong, L. and J. Tang. Strategies and Challenges on Selectivity of Photocatalytic Oxidation of Organic Substances. *Advanced Energy Materials*, **2021**, *11*, 2003216.
- [42] Lin, L., W. Zhou, R. Gao, S. Yao, X. Zhang, W. Xu, S. Zheng, Z. Jiang, Q. Yu, Y.-W. Li, C. Shi, X.-D. Wen, and D. Ma. Low-Temperature Hydrogen Production from Water and Methanol Using Pt/ α -MoC Catalysts. *Nature*, **2017**, *544*, 80.
- [43] Qiao, B., A. Wang, X. Yang, L.F. Allard, Z. Jiang, Y. Cui, J. Liu, J. Li, and T. Zhang. Single-Atom Catalysis of CO Oxidation Using Pt₁/FeO_x. *Nature Chemistry*, **2011**, *3*, 634.
- [44] Wang, C., K. Wang, Y. Feng, C. Li, X. Zhou, L. Gan, Y. Feng, H. Zhou, B. Zhang, X. Qu, H. Li, J. Li, A. Li, Y. Sun, S. Zhang, G. Yang, Y. Guo, S. Yang, T. Zhou, F. Dong, K. Zheng, L. Wang, J. Huang, Z. Zhang, and X. Han. Co and Pt Dual-Single-Atoms with Oxygen-Coordinated Co-O-Pt Dimer Sites for Ultrahigh Photocatalytic Hydrogen Evolution Efficiency. *Advanced Materials*, **2021**, *33*, 2003327.
- [45] Guo, W., Z. Wang, X. Wang, and Y. Wu. General Design Concept for Single-Atom Catalysts toward Heterogeneous Catalysis. *Advanced Materials*, **2021**, *33*, e2004287.
- [46] Zhang, W., Y. Chao, W. Zhang, J. Zhou, F. Lv, K. Wang, F. Lin, H. Luo, J. Li, M. Tong, E. Wang, and S. Guo. Emerging Dual-Atomic-Site Catalysts for Efficient Energy Catalysis. *Advanced Materials*, **2021**, *33*,

2102576.

- [47] Li, Q., Y. Ouyang, H. Li, L. Wang, and J. Zeng. Photocatalytic Conversion of Methane: Recent Advancements and Prospects. *Angewandte Chemie International Edition*, **2021**, 10.1002/anie.202108069.
- [48] Latimer, A.A., A. Kakekhani, A.R. Kulkarni, and J.K. Nørskov. Direct Methane to Methanol: The Selectivity–Conversion Limit and Design Strategies. *ACS Catalysis*, **2018**, *8*, 6894.
- [49] Shanmuganathan, V., J.S. Kumar, R. Pachaiappan, and P. Thangadurai. Transition Metal Ion-Doped In_2O_3 Nanocubes: Investigation of Their Photocatalytic Degradation Activity under Sunlight. *Nanoscale Advances*, **2021**, *3*, 471.
- [50] Xu, C.Y., P.X. Zhang, and L. Yan. Blue Shift of Raman Peak from Coated TiO_2 Nanoparticles. *Journal of Raman Spectroscopy*, **2001**, *32*, 862.
- [51] Siedl, N., P. Gügel, and O. Diwald. First Combined Electron Paramagnetic Resonance and Ft-Ir Spectroscopic Evidence for Reversible O_2 Adsorption on $\text{In}_2\text{O}_{3-x}$ Nanoparticles. *The Journal of Physical Chemistry C*, **2013**, *117*, 20722.
- [52] Reyes-Gil, K.R., Y. Sun, E. Reyes-García, and D. Raftery. Characterization of Photoactive Centers in N-Doped In_2O_3 Visible Photocatalysts for Water Oxidation. *The Journal of Physical Chemistry C*, **2009**, *113*, 12558.
- [53] García-Trenco, A., A. Regoutz, E.R. White, D.J. Payne, M.S.P. Shaffer, and C.K. Williams. Pd-In Intermetallic Nanoparticles for the Hydrogenation of CO_2 to Methanol. *Applied Catalysis B: Environmental*, **2018**, *220*, 9.
- [54] Wang, S., T. He, P. Chen, A. Du, K.K. Ostrikov, W. Huang, and L. Wang. In Situ Formation of Oxygen Vacancies Achieving near-Complete Charge Separation in Planar BiVO_4 Photoanodes. *Adv Mater*, **2020**, *32*, e2001385.
- [55] Zhu, W., M. Shen, G. Fan, A. Yang, J.R. Meyer, Y. Ou, B. Yin, J. Fortner, M. Foston, Z. Li, Z. Zou, and B. Sadler. Facet-Dependent Enhancement in the Activity of Bismuth Vanadate Microcrystals for the Photocatalytic Conversion of Methane to Methanol. *ACS Applied Nano Materials*, **2018**, *1*, 6683.
- [56] Wang, L., M. Ghossoub, H. Wang, Y. Shao, W. Sun, A.A. Tountas, T.E. Wood, H. Li, J.Y.Y. Loh, Y. Dong, M. Xia, Y. Li, S. Wang, J. Jia, C. Qiu, C. Qian, N.P. Kherani, L. He, X. Zhang, and G.A. Ozin. Photocatalytic Hydrogenation of Carbon Dioxide with High Selectivity to Methanol at Atmospheric Pressure. *Joule*, **2018**, *2*, 1369.
- [57] Chen, J., S. Stepanovic, A. Draksharapu, M. Gruden, and W.R. Browne. A Non-Heme Iron Photocatalyst for Light-Driven Aerobic Oxidation of Methanol. *Angewandte Chemie International Edition*, **2018**, *57*, 3207.

Declarations

Acknowledgements

L. L., L. F., H. L. and J. X. are grateful for the China Postdoctoral Science Foundation (Grant No. 2019M663802) and the Shannxi Key Research Grant (China, 2020GY-244). Y. X. and J.T. are thankful for financial support from the UK EPSRC (EP/S018204/2), Leverhulme Trust (RPG-2017-122), Royal Society Newton Advanced Fellowship grant (NAF\R1\191163 and NA170422) and Royal Society Leverhulme Trust Senior Research Fellowship (SRF\R1\21000153).

Author contributions

J.T. conceived and supervised the entire project. L. L., L. F. and H. L. conducted the material synthesis, characterizations and photocatalytic methane conversion tests. L. L. drafted the manuscript under the guidance of J. T.. Y. X. helped to discuss the catalytic results and improve the manuscript. All authors discussed and commented on the manuscript.

Competing interests

The authors declare no competing interests.

Scheme

Scheme 1 is in the supplementary files section.

Figures

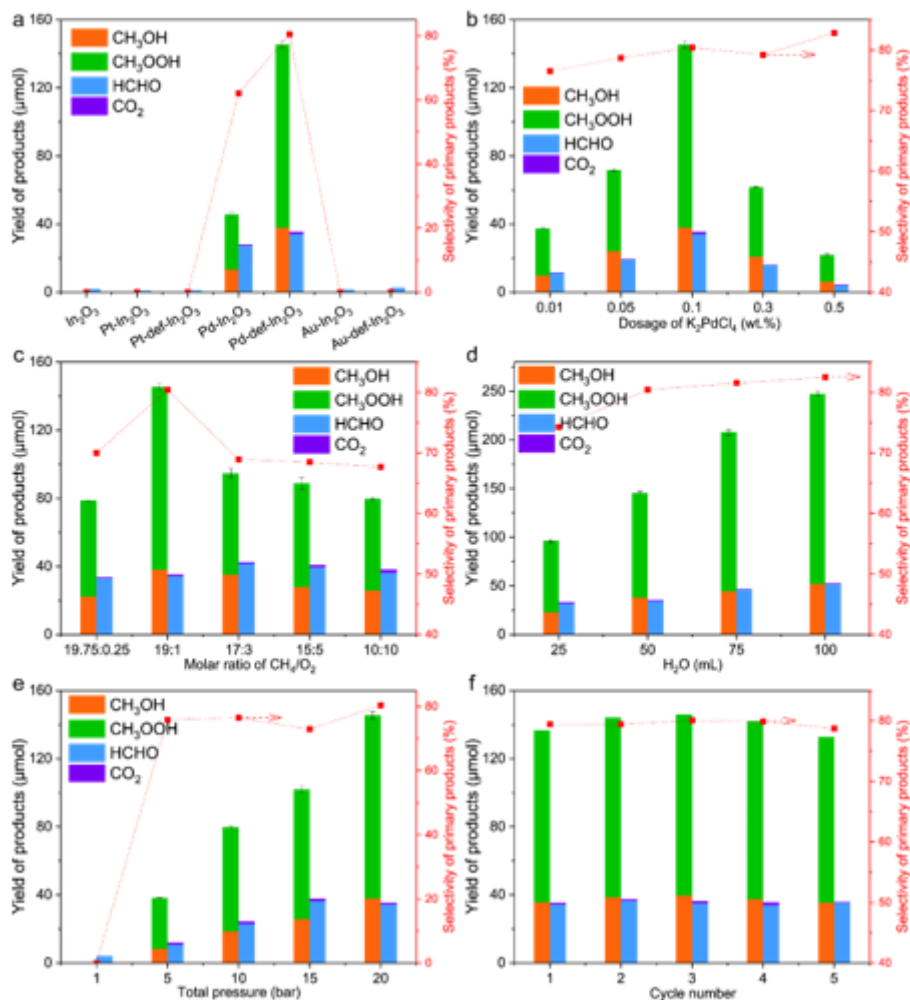


Figure 1

Photocatalytic CH₄ conversion performance under 420 nm irradiation. Investigations on (a) diverse noble metal species, (b) K₂PdCl₄ dosage during synthesis, (c) molar ratio of CH₄/O₂, (d) H₂O dosage, (e) total pressure and (f) cycling tests over the best sample Pd-def-In₂O₃. Standard reaction conditions: 20 mg photocatalyst, 50 mL distilled H₂O, 19 bar CH₄, 1 bar O₂, 3 h. For reaction condition investigation, only the specified parameter was changed.

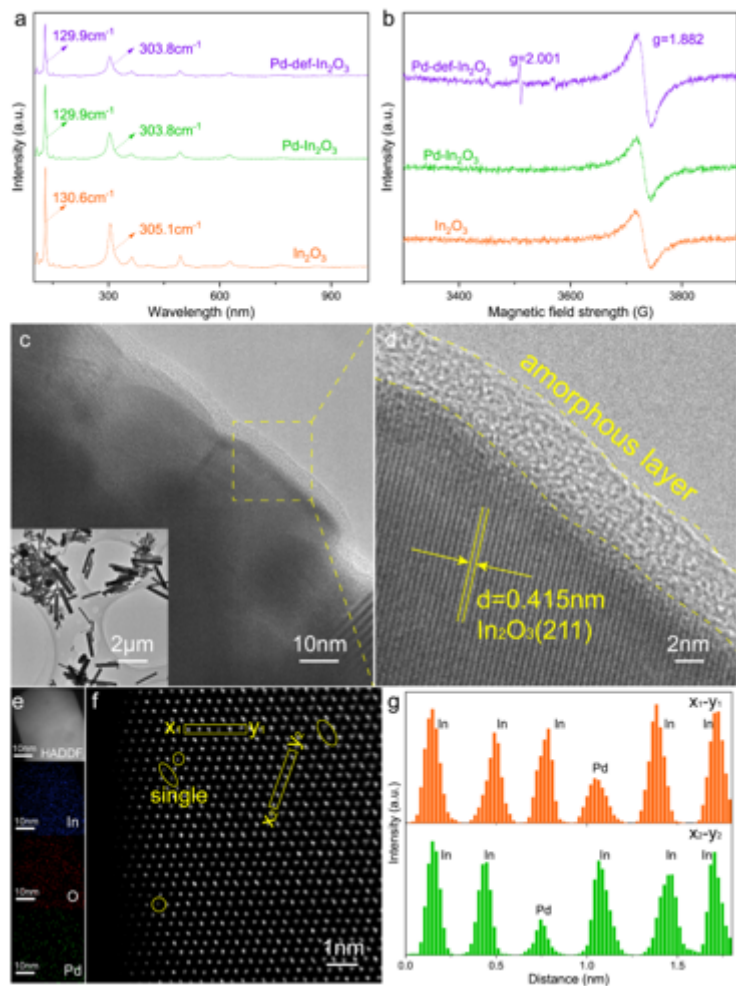


Figure 2

(a) Raman and (b) EPR spectra of In_2O_3 , $\text{Pd-In}_2\text{O}_3$ and $\text{Pd-def-In}_2\text{O}_3$. (c, d) HRTEM and (e) HAADF and EDS-mapping images of $\text{Pd-def-In}_2\text{O}_3$. Blue, red and green colors represent indium, oxygen and palladium elements, respectively. (f) Aberration corrected HAADF-STEM image of $\text{Pd-def-In}_2\text{O}_3$, where Pd single atoms with a weak intensity are indicated by yellow circles. (g) Line scan measured along the x-y rectangle region marked in f.

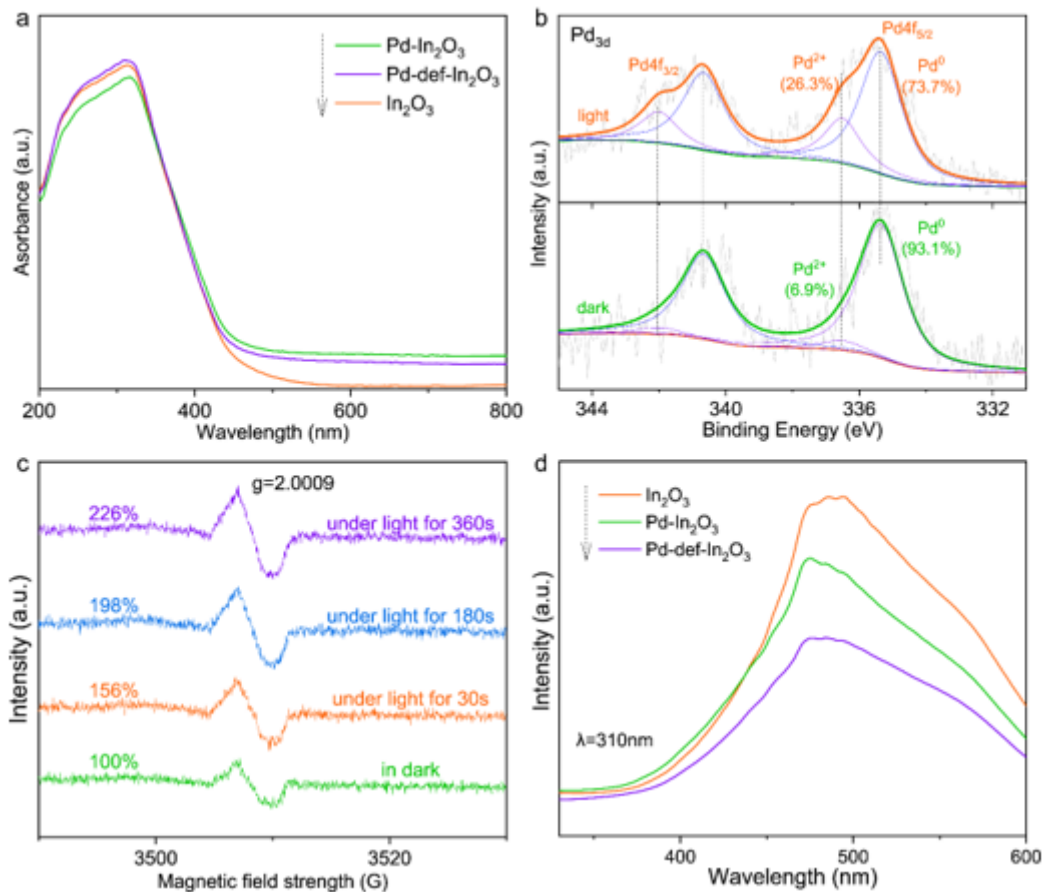


Figure 3

(a) UV-DRS spectra of In₂O₃, Pd-In₂O₃ and Pd-def-In₂O₃. (b) In-situ Pd 3d XPS spectra and (c) in-situ EPR spectra of Pd-def-In₂O₃ in dark and under light. (d) Steady-state PL spectra of In₂O₃, Pd-In₂O₃ and Pd-def-In₂O₃.

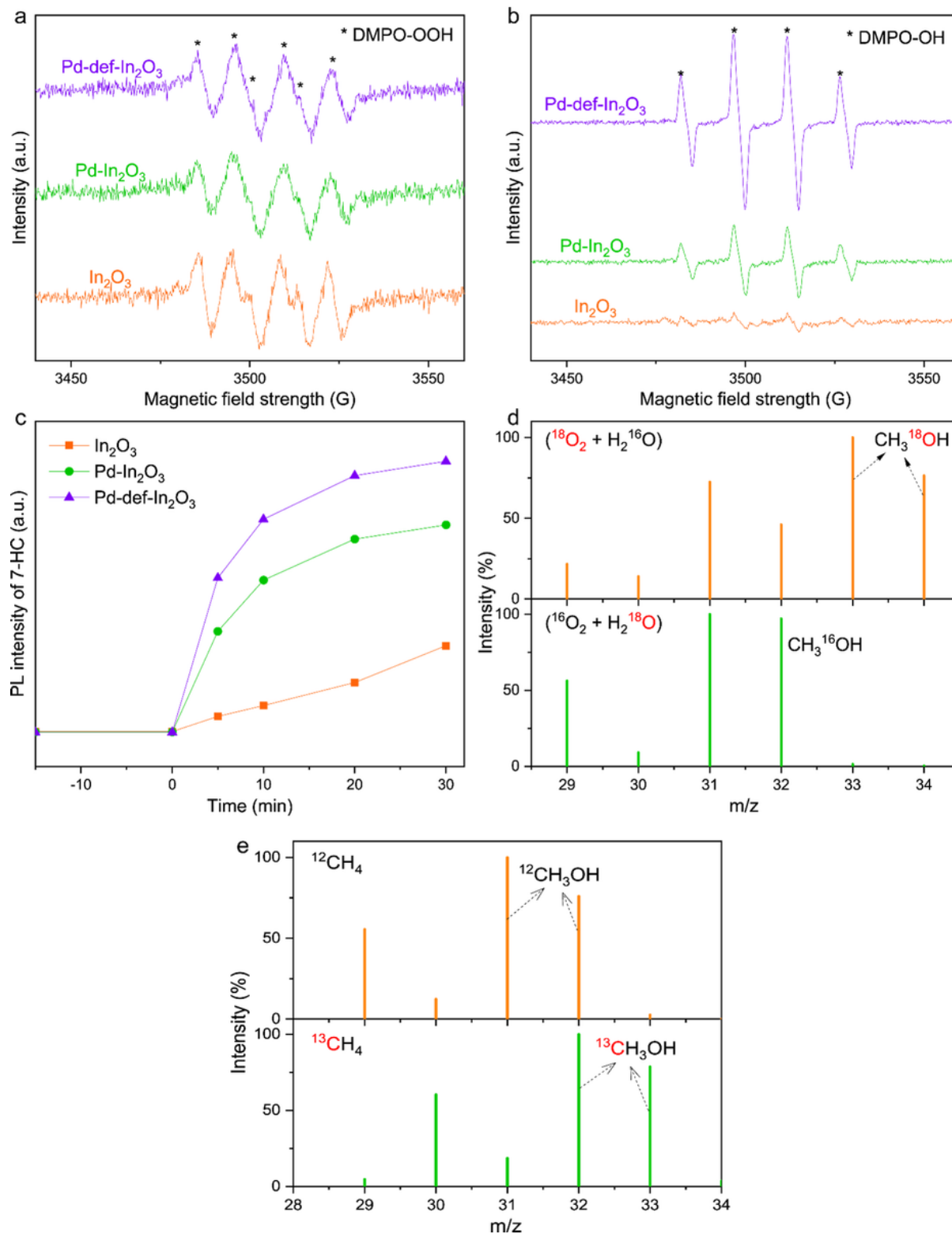


Figure 4

In-situ EPR spectra of (a) DMPO-OOH and (b) DMPO-OH for the monitor of reactive ·OOH and ·OH radicals over different photocatalysts. (c) PL intensity of 7-HC versus time over different photocatalysts for the quantification of ·OH. Isotopic labelled experiments (d) oxygen source and (e) carbon source for methanol production in the presence of isotopic labelled H₂¹⁸O, ¹⁸O₂ or ¹³CH₄.

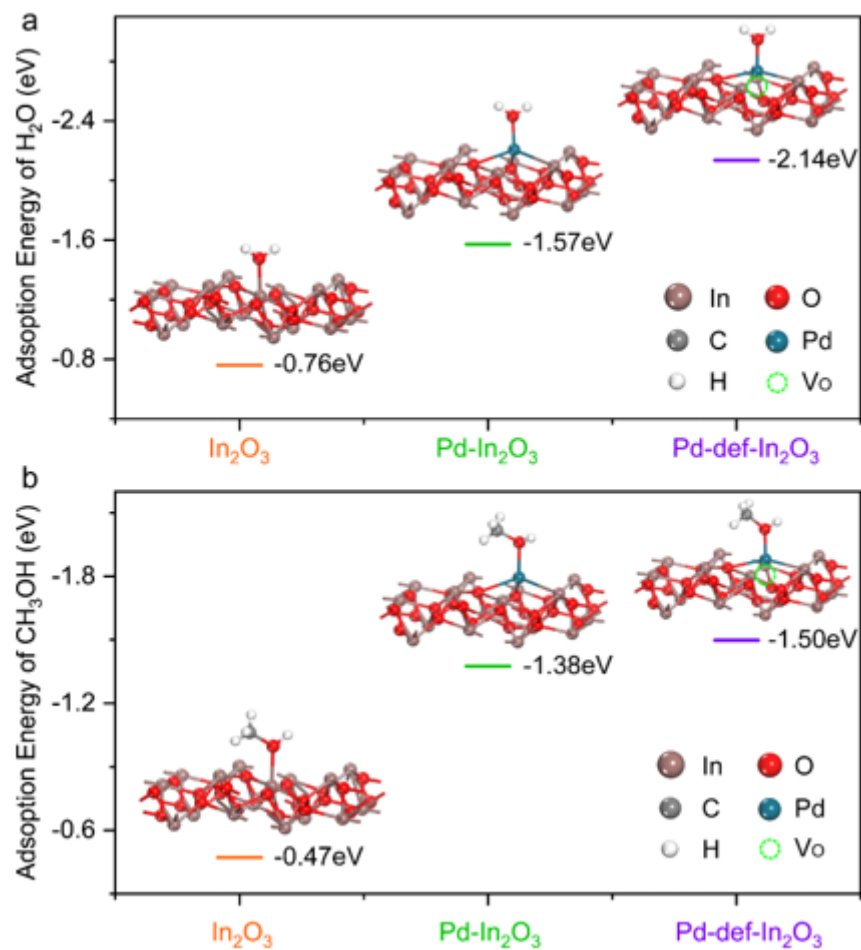


Figure 5

DFT calculation of optimized geometries and adsorption energies of (a) H₂O and (b) CH₃OH on In₂O₃, single atom Pd-In₂O₃ and Pd-def-In₂O₃.

Supplementary Files

This is a list of supplementary files associated with this preprint. Click to download.

- [Scheme1.png](#)
- [supportinginformation.docx](#)